

Multiparameter full-waveform inversion of data from the Valhall field

Nishant Kamath^{1*}, Romain Brossier¹, Ludovic Métivier², & Pengliang Yang³

¹ISTerre, Université Grenoble-Alpes

^{1,2}LJK, CNRS, Université Grenoble-Alpes

³EMGS, Norway

SUMMARY

It has been shown that full-waveform inversion (FWI) of data acquired in regions where the medium is known to be viscous yields distorted velocities if attenuation is not taken into account. In the case of velocity-only inversion in visco-acoustic media, the sensitivity of the inverted velocity to the values of attenuation must be investigated. When velocity and attenuation Q_p are simultaneously updated, the choice of the gradient preconditioner could influence the final result. Here, we perform visco-acoustic FWI of ocean bottom cable (OBC) dataset from the Valhall field. Monoparameter (velocity-only) inversion with different Q_p models yields velocities which are very similar to each other. Simultaneous inversion of velocity and Q_p with the same preconditioner used in the monoparameter case results in small differences in the obtained velocity. However, a modified wavefield preconditioner improves the inverted velocity and attenuation significantly.

INTRODUCTION

The inherent tradeoffs between model parameters and how they influence the objective function, in terms of sensitivity, make multiparameter full-waveform inversion (FWI) a challenging problem (Virieux and Operto, 2009; Malinowski et al., 2011; Virieux et al., 2017). Particularly in the case of simultaneous inversion of velocity and attenuation, both the parameters have isotropic radiation patterns (Yang et al., 2018). Although, the $\pi/2$ phase-shift introduced by attenuation Q_p mitigates the coupling between the parameters, an appropriate preconditioner, which approximates an inverse Hessian could help better resolve the parameters (Yang et al., 2018).

Based on synthetic tests, Malinowski et al. (2011) conclude that the objective function is less sensitive to attenuation (compared to velocity) as the value of Q_p in the medium increases. However, simultaneous inversion for a broad range of frequencies enables successful reconstruction of both the parameters to a similar resolution. Operto and Miniussi (2018) perform multiparameter frequency-domain FWI to invert ocean bottom cable (OBC) data from the Valhall field. Compared to the inverted density ρ , velocity and Q_p are more reliably updated. The velocity and Q_p models obtained by inverting data from the North Sea are shown by Wang et al. (2018) to yield Q-compensated migration images which have consistent amplitudes and better-resolved events.

Here, we invert the pressure component of Ocean Bottom Cables (OBC) data from the Valhall field, different from those from Operto and Miniussi (2018). A spatially varying attenuation field and one with constant values of Q_p are used to

perform velocity-only updates. For the multiparameter (V_{p0} and Q_p) inversion, we compare depth and a modified wavefield preconditioner.

MODEL AND DATA

The Valhall field exhibits VTI (transverse isotropy with a vertical symmetry axis), with values of ϵ and δ reaching up to 0.2 and 0.08, respectively. The chalk reservoir, at a depth of 2.5 km makes velocity estimation underneath it a challenging problem. The presence of low-velocity anomalies in the sediments overlaying the reservoir is indicative of gas clouds (Barkved et al., 2010), making the medium attenuative. The water bottom is at a constant depth of 70 m. The initial P-wave vertical velocity V_{p0} , and the anisotropy coefficient ϵ , computed through conventional tomography, and the parameter δ obtained from well ties, were provided to us by AkerBP (Figure 1). We use Gardner's relationship to build the density model from the provided velocity field.

The multicomponent OBC data acquired by AkerBP in 2011 consists of thirteen cables (2048 receivers), 300 m apart and 50,824 shots which were at a depth of 5 m. The survey covers an area of approximately 145 square km, and the shot- and receiver- spacing are 50 m each. We were provided raw SEG-Y data and we performed the following steps to prepare them for FWI: rotation and translation of the data to the computation grid, application of source-receiver reciprocity, removal of spiky traces, and minimum-phase filtering to divide the data into two sets of frequency bands (2.5 – 5 Hz and 2.5 – 7 Hz). Only the hydrophone component is employed in the inversion.

FWI METHODOLOGY

The equations that approximate propagation of acoustic waves in VTI media (Duvenceck and Bakker, 2011) are discretised (4th order in space and 2nd order in time) to generate the wavefield. Three standard linear solid (SLS) mechanisms (Yang et al., 2018) are employed to simulate constant attenuation for the given range of frequencies. In attenuative media, the stiffness coefficients and, hence, the velocity, is frequency dependent. However, we formulate the equations in such a way that the velocity and Q_p are decoupled, and the velocity itself corresponds to the unrelaxed moduli, i.e., those at infinite frequencies. The checkpoint-assisted reverse forward simulation (CARFS) technique (Yang et al., 2016) is employed to obtain the gradient of the objective function with respect to the model parameters.

The model updates every iteration are performed by the preconditioned l -BFGS algorithm implemented in the SEISCOPE

Multiparameter FWI of Valhall data

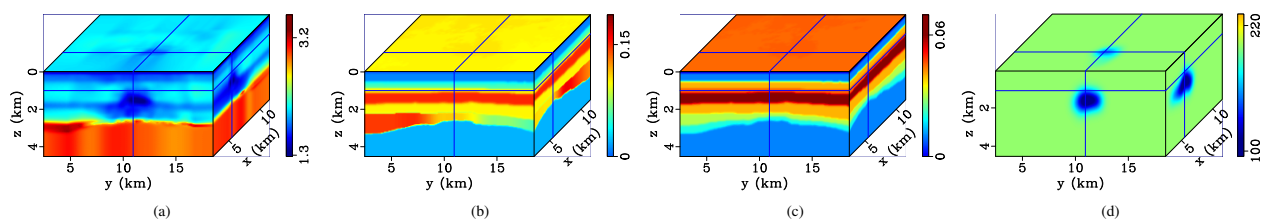


Figure 1: Initial (a) P-wave vertical velocity V_{P0} , and the anisotropy coefficients (b) ϵ and (c) δ , and (d) the spatially-varying attenuation model Q_P used for monoparameter FWI. Here, and in subsequent plots of attenuation, we start from 0.1 km to avoid displaying large values in the water column.

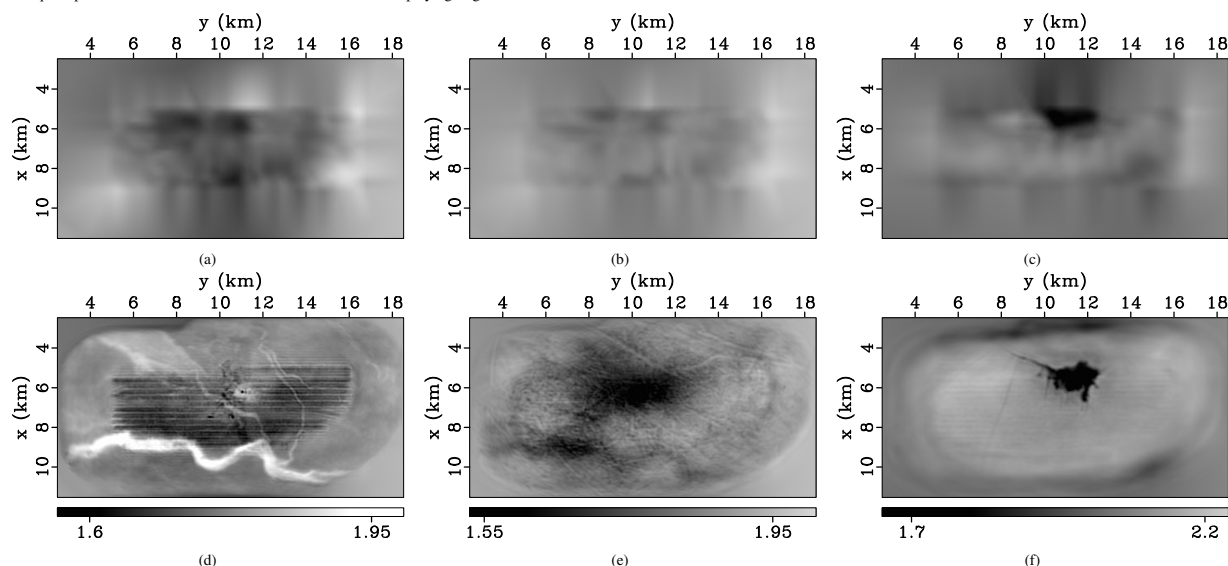


Figure 2: Initial P-wave vertical velocity V_{P0} at depths of (a) 200 m, (b) 500 m, and (c) 1000 m. The V_{P0} obtained from monoparameter FWI starting with a constant Q_P -model. The units of velocity here, and in the following figures are km/s.

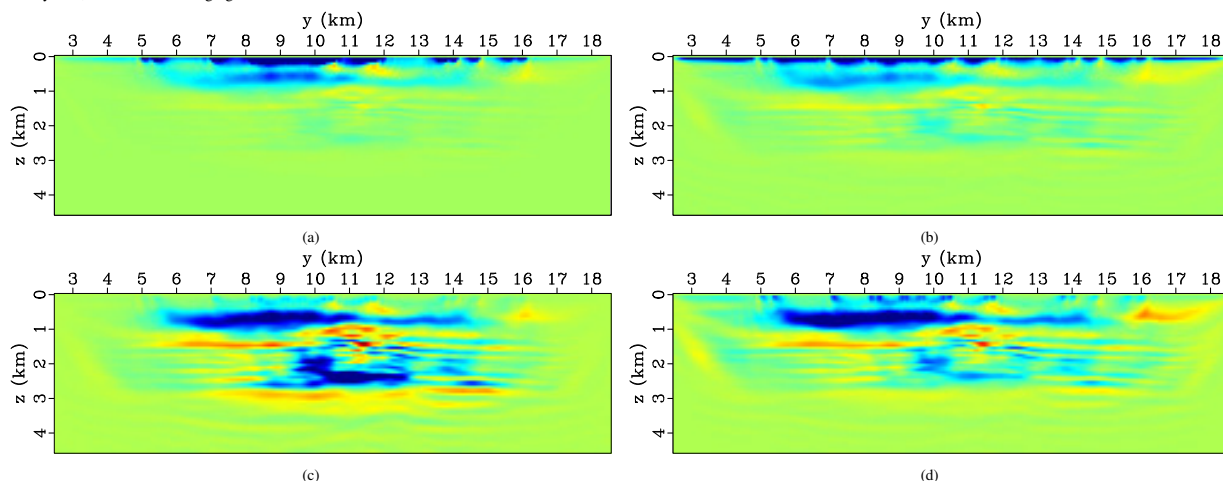


Figure 3: Gradient of the objective function with respect to V_{P0} (a) without any preconditioning, (b) with wavefield preconditioning, (c) with depth preconditioning, and (d) with modified wavefield preconditioning.

optimization toolbox (Métivier and Brossier, 2016). It is essential to apply an appropriate preconditioner to the gradient to help the inversion converge faster to the actual solution and, in the case of multiparameter inversion, to try and decouple the model parameters. The depth preconditioner used here simply weights the gradient by a function of depth. A more sophisticated preconditioner, which consists of the source wavefield weighted by the scattering matrix, was shown to better

account for the tradeoffs between the various model parameters for FWI in a synthetic 2D experiment (Yang et al., 2018). However, it involves tuning multiple parameters: to scale the model parameter updates relative to each other, and to balance the amplitudes as a function of depth within each parameter. The updates are, however, very sensitive to the tuning parameters and, in addition, require several trials to ascertain. Hence, in our work, we apply a modified version of the source wavefield

Multiparameter FWI of Valhall data

preconditioner (explained later).

To use all available data without sacrificing efficiency, we employ the data sub-sampling strategy outlined in Kamath et al. (2018) during FWI: three iterations of *l*-BFGS are run on a random selection of 128 shots, without repetition, until all the shots are included in the inversion.

FWI RESULTS

Monoparameter inversion

In order to investigate the sensitivity of the objective function to attenuation, we run monoparameter (V_{P0} -only) visco-acoustic FWI for two different Q_p models: the first is spatially varying and has values of 1000 in the water column, 100 in the sediments (where $V_{P0} < 1600$ m/s), and 200 elsewhere (Figure 1d). The second model, henceforth referred to as the constant- Q_p model, is such that $Q_p = 1000$ in the water column and has values of 200 in the sediments. Depth preconditioning is employed in both the cases.

The V_{P0} -fields obtained from the constant and spatially varying Q_p differ by less than 2% for the depths shown in Figure 2, in spite of the Q_p models being quite different. In both cases, however, the velocities are updated significantly: the shallow, underground channel-like morphologies are clearly visible, and the gas cloud at $z = 1000$ m is well delineated.

Multiparameter inversion

A depth preconditioner of z^2 , where z represents depth, was tested and found to be too strong in the deeper regions, whereas z^1 , employed here, performed better. A preconditioner which is constructed from the source and/or receiver wavefields would better account for spatial variations in the model. The technique outlined in Yang et al. (2018), although promising in terms of resolving different parameter classes (such as V_{P0} and Q_p), was found to be too sensitive to the tuning parameters. The source (or receiver) wavefield, squared and summed over time, and applied as a gradient preconditioner, balances the gradient amplitudes as a function of depth (Shin et al., 2001). The sparse shot-sampling, however, used in our work, causes problems with the last two techniques.

Figure 3a is the gradient with respect to V_{P0} along $x = 5.6$ km, computed during the first iteration. The preconditioned gradient (Figure 3b) computed from the source wavefield has large amplitudes close to the surface and is not very different from the gradient. Preconditioning it by z^1 (Figure 3c) tends to strengthen the amplitudes in the deeper region too much. To enable the use of the wavefield preconditioner while, at the same time, ensuring that the amplitudes close to the surface are not too high, we modify it such that the values to a depth of $z = 0.8$ km are computed from the depth preconditioner, resulting in the preconditioned gradient shown in Figure 3d.

The modified wavefield preconditioner decreases the acquisition footprint in the inverted V_{P0} significantly (compare Figures 4a and 4d). It also improves the resolution of the low-velocity anomaly (Figure 4f). The velocities at the depth slices shown

here vary by up to 2%, although locally, the differences go as high as 10%. The improvement in horizontal continuity is also noticeable, for example, at $z = 1$ km (Figure 5c).

Interestingly, there are small differences up shallow between the V_{P0} obtained from monoparameter and simultaneous inversion using the same (depth) preconditioner (compare Figures 2d and 4a and Figures 2e and 4b). At $z = 1000$ m, however, the differences are insignificant.

The inverted attenuation up shallow ($z = 200$ m) is more localised, as apparent from the extent of the low Q_p values in Figure 4j (compared to Figure 4g). Similar results are noticed around the low-velocity anomaly, at $z = 1000$ m. Interestingly, the largest differences in the values of Q_p are observed at $z = 500$ m ($\approx 5\%$, and locally as large as 13%). We notice some correlation between low values of velocities and attenuation, especially at depths of 500 m and 1000 m. The lower Q_p values surrounding the anomaly at $z = 1000$ m could be artefacts. The slices at $x = 5.6$ km display significant differences in the inverted attenuation fields (compare Figures 5e and 5f). Images and image gathers obtained from migrating the data with the inverted models should help judge the accuracy of the models.

CONCLUSIONS

Here, we use a shot sub-sampling strategy to invert 3D OBC dataset from the Valhall field. Frequencies of up to 7 Hz in the data are employed in the inversion and a preconditioned *l*-BFGS algorithm performs the model updates.

Monoparameter visco-acoustic FWI for the P-wave vertical velocity V_{P0} does not seem to be very sensitive to the attenuation model. However, differences in the velocities obtained from mono and multiparameter inversion using the same (depth) preconditioner are noticeable, especially up shallow.

The source wavefield preconditioner is modified in order to account for the sparse shots resulting from the subsampling strategy, and to ensure appropriate amplitude compensation of the gradient as a function of depth. The modified preconditioner results in significant improvement (over depth preconditioner) in V_{P0} and attenuation Q_p obtained from simultaneous inversion, both up shallow and in the deeper region, where the low-velocity anomaly exists.

The next step would be to migrate the data with the obtained velocity and attenuation models to better estimate the accuracy of the inverted models.

ACKNOWLEDGMENTS

This study was partially funded by the SEISCOPE consortium (<http://seiscope2.osug.fr>), sponsored by AKERBP, CGG, CHEVRON, EXXON-MOBIL, JGI, PETROBRAS, SCHLUMBERGER, SHELL, SINOPEC, STATOIL and TOTAL. This study was granted access to the HPC resources of SIGAMM infrastructure (<http://crimson.oca.eu>) and CINES/IDRIS/TGCC under the allocation 046091 made by GENCI. We appreciate AKERBP ASA and their partner Pandion Energy for providing the dataset and permission to publish this work, and the comments of Ross Milne from AKERBP.

Multiparameter FWI of Valhall data

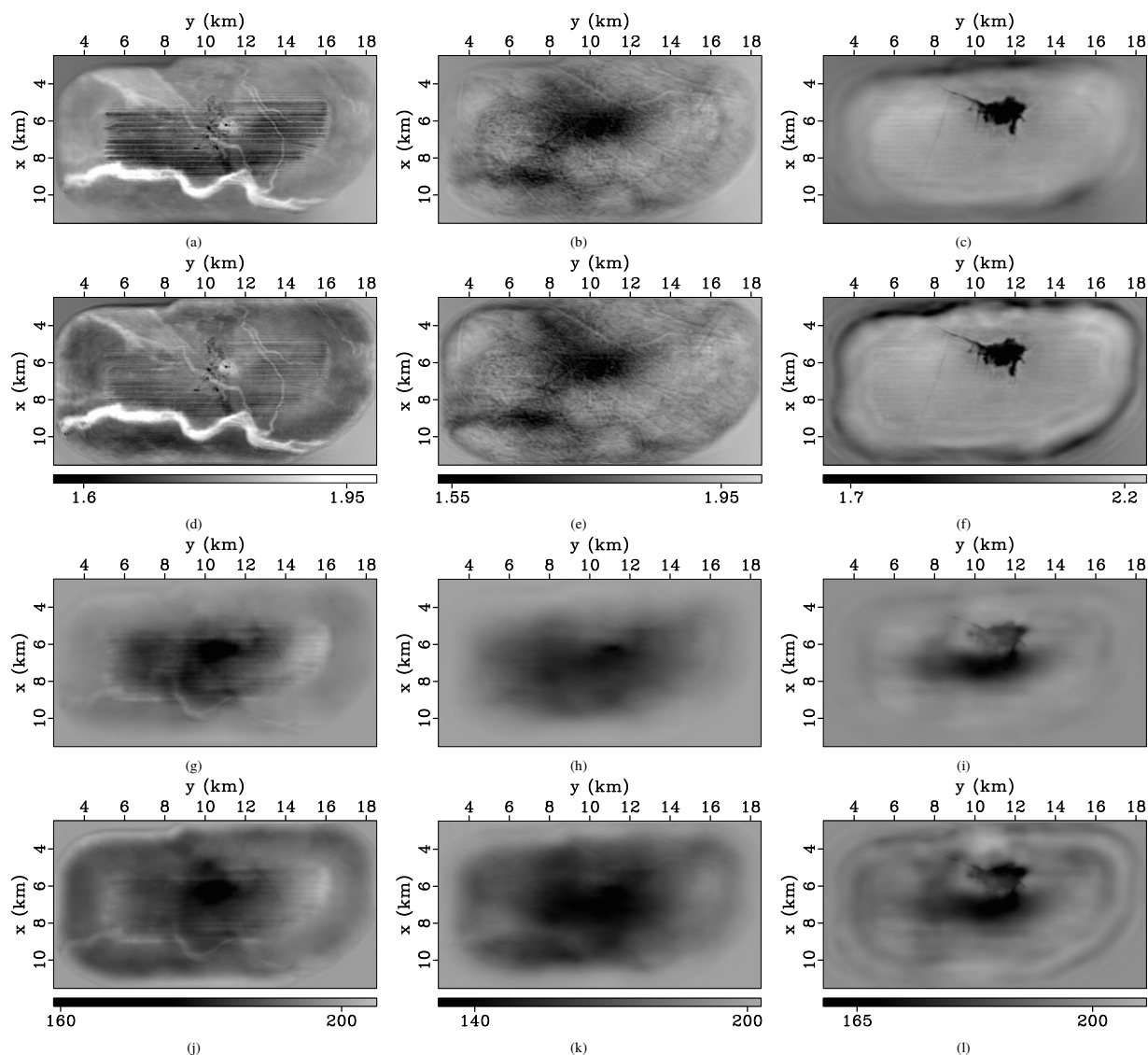


Figure 4: Inverted P-wave vertical velocity V_{P0} at depths of (a) 200 m, (b) 500 m, and (c) 1000 m from multiparameter FWI, using depth preconditioning. The V_{P0} obtained at (d) $z = 200$ m, (e) $z = 500$ m, and (f) $z = 1000$ m by employing the modified source wavefield preconditioner. The Q_P at depths of (g) 200 m, (h) 500 m, and (i) 1000 m, from depth preconditioning, and those from the wavefield preconditioning at (j) $z = 200$ m, (k) $z = 500$ m, and (l) $z = 1000$ m.

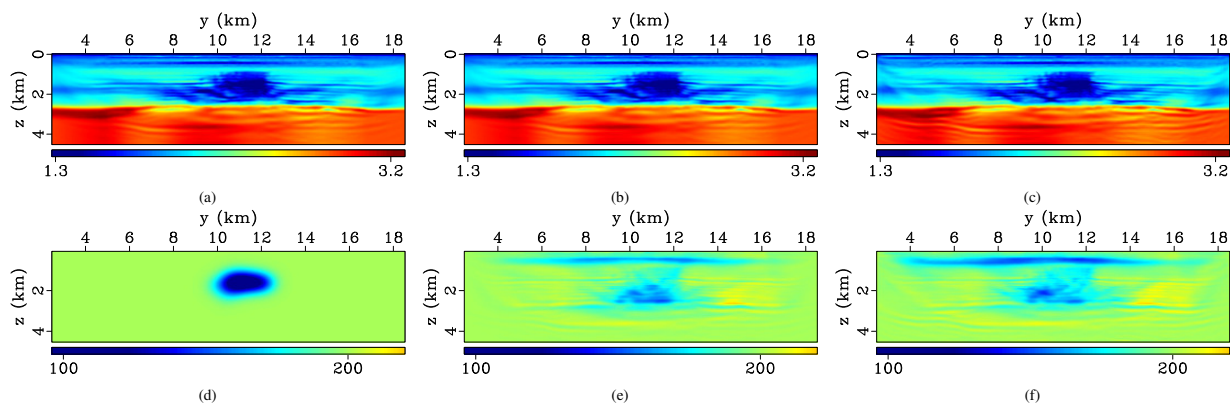


Figure 5: Velocity V_{P0} at $x = 5.6$ km obtained from (a) monoparameter inversion using spatially varying attenuation, and simultaneous inversion with (b) depth preconditioner, and (c) modified wavefield preconditioner. (d) The Q_P model employed in the monoparameter inversion, and those obtained from simultaneous inversion using (e) depth preconditioner, and (f) wavefield preconditioner.

REFERENCES

- Barkved, O., P. Heavey, J. H. Kommedal, J.-P. van Gestel, R. S. Ve, H. Pettersen, C. Kent, and U. Albertin, 2010, Business impact of full waveform inversion at valhall: 80th Annual International Meeting, SEG, Expanded Abstracts, **29**, 925–929, doi: <https://doi.org/10.1190/1.3513929>.
- Duveneck, E., and P. M. Bakker, 2011, Stable P-wave modeling for reverse-time migration in tilted TI media: *Geophysics*, **76**, no. 2, S65–S75, doi: <https://doi.org/10.1190/1.3533964>.
- Kamath, N., R. Brossier, L. Métivier, and P. Yang, 2018, 3d acoustic/viscoacoustic time-domain FWI of OBC data from the Valhall field: 88th Annual International Meeting, SEG, Expanded Abstracts, 1093–1097, doi: <https://doi.org/10.1190/segam2018-2997017.1>.
- Malinowski, M., S. Operto, and A. Ribodetti, 2011, High-resolution seismic attenuation imaging from wide-aperture onshore data by visco-acoustic frequency-domain full wave- form inversion: *Geophysical Journal International*, **186**, 1179–1204, doi: <https://doi.org/10.1111/j.1365-246X.2011.05098.x>.
- Métivier, L., and R. Brossier, 2016, The seiscopes optimization toolbox: A large-scale nonlinear optimization library based on reverse communication: *Geophysics*, **81**, no. 2, F11–F25, doi: <https://doi.org/10.1190/geo2015-0031.1>.
- Operto, S., and A. Miniussi, 2018, On the role of density and attenuation in 3D multi-parameter visco-acoustic VTI frequency-domain FWI: an OBC case study from the North Sea: *Geophysical Journal International*, **213**, 2037–2059, doi: <https://doi.org/10.1093/gji/ggy103>.
- Shin, C., S. Jang, and D. J. Min, 2001, Improved amplitude preservation for prestack depth migration by inverse scattering theory: *Geophysical Prospecting*, **49**, 592–606, doi: <https://doi.org/10.1046/j.1365-2478.2001.00279.x>.
- Virieux, J., A. Asnaashari, R. Brossier, L. Métivier, A. Ribodetti, and W. Zhou, 2017, An introduction to Full Waveform Inversion, in *Encyclopedia of Exploration Geophysics*: SEG, R1-1–R1-40.
- Virieux, J., and S. Operto, 2009, An overview of full waveform inversion in exploration geophysics: *Geophysics*, **74**, no. 6, WCC1–WCC26, doi: <https://doi.org/10.1190/1.3238367>.
- Wang, M., Y. Xie, B. Xiao, A. Ratcliffe, and T. Latter, 2018, Visco-acoustic full-waveform inversion in the presence of complex gas clouds: 88th Annual International Meeting, SEG, Expanded Abstracts, 5516–5520, doi: <https://doi.org/10.1190/segam2018-w23-01.1>.
- Yang, P., R. Brossier, L. Métivier, and J. Virieux, 2016, Wave- field reconstruction in attenuating media: A checkpointing-assisted reverse-forward simulation method: *Geophysics*, **81**, no. 6, R349–R362, doi: <https://doi.org/10.1190/geo2016-0082.1>.
- Yang, P., R. Brossier, L. Métivier, J. Virieux, and W. Zhou, 2018, A time-domain preconditioned truncated Newton approach to multiparameter visco-acoustic full waveform inversion: *SIAM Journal on Scientific Computing*, **40**, B1101–B1130, doi: <https://doi.org/10.1137/17M1126126>.